Desalination and Water Treatment
www.deswater.com
doi: 10.1080/19443994.2014.939492

55 (2015) 3310–3329
September

Taylor & Francis
Taylor & Francis Group

Thermal desalination and air conditioning using absorption cycle

Hassan K. Abdulrahim*, Mohamed A. Darwish

Qatar Environment and Energy Research Institute (QEERI) – Qatar Foundation, PO Box 5825, Doha, Qatar, email: habdelrehem@qf.org.qa

Received 30 March 2014; Accepted 16 June 2014

ABSTRACT

Water shortage and hot climate are the most stressing problems in many places all over the world, especially in the Arabian Gulf region. Efficient and sustainable solutions for these problems are a real challenge facing the Gulf Co-operating Countries countries. Vapor absorption cycles have been used for refrigeration and air conditioning application many years ago. The absorption cycle systems are a heat-driven system that can be used as a refrigerator, a heat pump, or a heat transformer. In this work, a new configuration of an absorption cycle has been used to provide chilled water for air conditioning applications and to supply saturated steam to a thermal desalination unit using solar radiation as the driving energy for the cycle. Water–Lithium Bromide absorption cycle is adapted. A low temperature, multi-effect distillation system is combined with the absorption cycle. The combined absorption-desalination systems are modeled and simulated using IPSEpro software.

Keywords: Solar cooling; Absorption cycle; Water-Lithium Bromide; Multi-effect distillation; Horizontal tube falling film evaporation

1. Introduction

Water scarcity and high hot summer temperatures are two predominant problems facing most areas of the Gulf Co-operating Countries (GCC) council including Saudi Arabia (SA), Kuwait, Qatar, United Arab Emirates, Bahrain, and Oman. As an example, Qatar has almost no natural water resources and about 50°C prevailing temperatures most of summer days. These two problems have to be sustainably solved to sustain life in the GCC. Water scarcity is solved for the time being by desalting seawater, that consumes much energy and negatively affecting the environment. Desalted seawater (DW) represents 99% of potable water in Qatar and 93% in Kuwait, as examples. On the other hand, summer high temperatures are solved mainly by summer air conditioning (AC) of most buildings. Extensive amounts of fossil fuel, e.g. natural gas (NG) and oil are consumed to secure the energy needs for DW production and AC operation. The oil and NG resources are finite and depleting. Summer AC load consumes at least 67% of the electric power (EP) during summer peak load in these countries. Desalination process is performed in co-generation power desalting plants (CPDP), and is typically responsible for up to 25% of the fuel consumed in

*Corresponding author.

Presented at the Conference on Desalination for the Environment: Clean Water and Energy, 11–15 May 2014, Limassol, Cyprus

these CPDP. Most recent power plants (PP) and/or CPDP are using gas Turbines (GT) and GT combined cycle (GTCC). The GT and GTCC plants are preferably operated by NG. When the amounts of the available NG is not enough, oil is used; as in SA and Kuwait. The NG is a cleaner fuel with less polluting gases when compared to oil, and the NG prices are much lower than that of oil. Therefore, NG is the main fuel used in PP to generate the EP required for operating the AC equipment, and to generate DW in CPDP.

Although, the GCC have huge NG resources (about 28% of the world), there is a serious shortage of the available NG needed to run their PP due to continually rising EP consumption, except in Qatar. The NG demand is much more than the region's gas exploration and production, and NG has to be imported, [1]. The growing shortage in NG in the GCC is due to, [1]; increasing power consumption and high share of NG in EP generation; depleting oil fields with need for gas to enhance oil recovery, increasing economic emphasis on petrochemicals, steel, and aluminum sectors; gas exploration and production challenges; and long-term NG export commitments limiting local supply. The NG production and consumption in the GCC and Iran are given in Table 1.

As mentioned before, oil is much more expensive and it has also better usage than being burned in power plants. While all NG productions are almost consumed in all GCC, except Qatar, oil production in the GCC can be fully consumed within two or three decades if the same consumption rates prevail.

The GCC should look for sustainable prime energy source such as solar energy to generate DW to provide potable water, and EP needed to operate AC systems. Solar energy is an attractive solution for operating AC systems. It saves electricity and thus primary energy sources (NG or oil), and decreases the emission of air-polluting gases and greenhouse gases (GHG) causing global warming. The AC cooling loads and the available solar power match well with each other along the day and seasons. Therefore, solar AC also leads to reducing the peak EP demand, and thus reduces the initial cost used due to the expensive peak electricity.

1.1. Air conditioning and EP peak demand

Presently, most of AC systems in the GCC are operating with mechanical vapor compression (MVC) refrigeration systems. Fig. 1 shows the ideal cycle of this system, which is driven by EP. The EP is consumed, mainly, by the compressor. Small fractions of EP are used by evaporator and condenser fans for heat addition and removal processes in air-cooled systems; as shown in Fig. 1; or water pumps and fans for cooling tower in water-cooled systems.

1.2. The role of AC in peak EP demand

The GCC experienced rapid development of economic and urban construction and therefore the use of AC is continuously on the rise. The GCC heating, ventilation, and air conditioning (HVAC) market demands are high where it crossed $6 billion in 2012 as shown in Fig. 2, [3]. All air conditioners in the GCC are using the electric-driven MVC refrigeration system. The electric power (EP) load is directly related to the outside air temperature, and thus with buildings' AC cooling load. The effect of AC cooling load on the EP production can be shown by the EP load in one of the hot summer days, when the AC equipment are fully running, and in winter days when no AC equipment is operated. Fig. 3 shows the load on 14 July 2010 when the maximum load reached 5,090 MW in Qatar, while on 8 February 2010, the minimum load reached 1,570 MW, [4]. Similar pattern prevails in all other GCC. This means that the capacity (or load)

Table 1
NG supply and consumption in BCF by the GCC and Iran during 2011, [2]

Country	Production BCF	Consumption BCF	Import/export	Reserve TCF
Qatar	4,121	690	4,015	899
Bahrain	446	446	NA	3
Iran	5,361	5,415	−54	1,046
Kuwait	478	502	−24	64
Oman	937	619	317	30
Saudi Arabia	3,258	3,504	NA	264
United Arab Emirates	1,847	2,663	−433	214
Total	16,448	13,839		2,520
Total without Iran	11,087	8,424		1,474

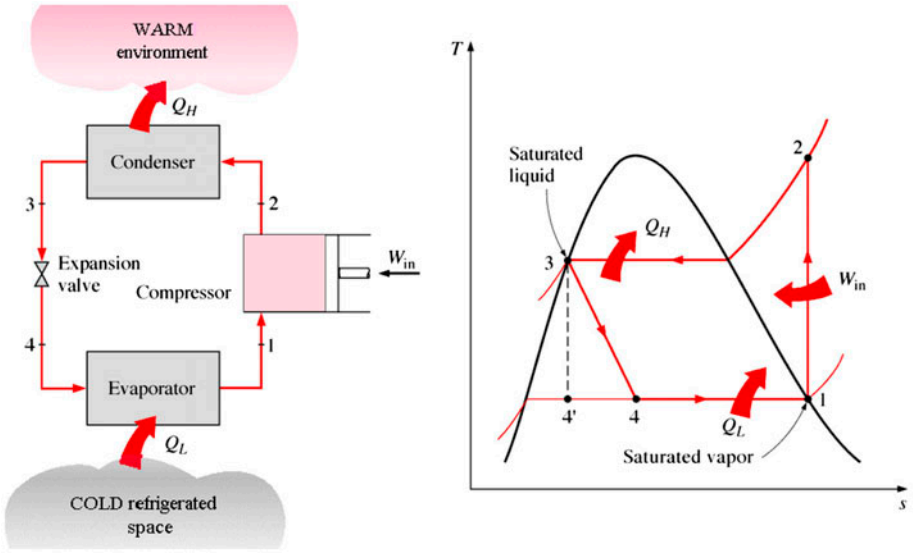

Fig. 1. Mechanical vapor compression system using Refrigerant 134A and electrically-driven compressor.

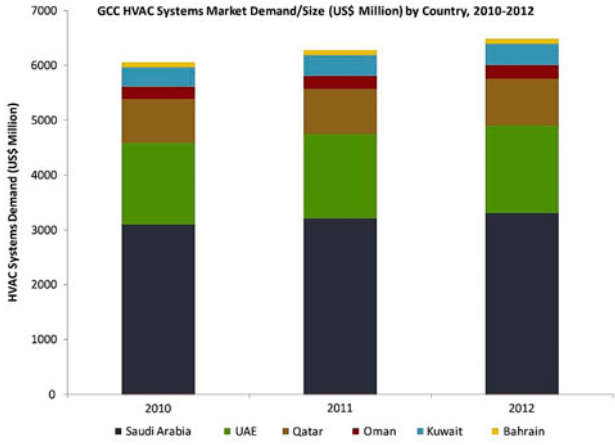

Fig. 2. HVAC market in the GCC, [3].

factor is very low in winter, and thus the power plants capacity is underutilized significantly in winter. It means also that additional EP plant capacity is mainly needed to secure the summer peak load because of the AC load; and not for the average load. The capacity factor of a power plant is the ratio of the actual output of a power plant over a period of time and its potential output if it had operated at full nameplate capacity during that time. Fig. 4 shows the change in the EP load in one summer day in Kuwait due to the change of the AC cooling load along the day from 5,750 MW at early morning (6:00 am) to 7,480 MW in the afternoon (at 15:00 pm). Table 2 shows the maximum and minimum EP load from 2006 to 2010 in Qatar, [5]. Therefore, the AC equipment is contributing directly to the summer peak power demand. Increased peak electricity demand has become one of the most serious problems faced by the GCC.

The increased peak demand is many times the base generation load. As a result, there is an increase in electricity cost due to the need for the installation of peaking power plants, which serve for very short periods annually, normally during the peak summer days. Supplying the ever-increasing peak load requires the installation of more and more generating infrastructure, such as transmission infrastructure necessary to cope with the peak demand at great cost. If the electricity supply does not meet demand, then grid failures result. This is expensive in terms of network damage, lost productivity, and loss of essential services.

Solar air conditioning is an excellent viable solution to turn the severe summer heat in the GCC into cooling. It also improves the environment by limiting the air-polluting gases and GHG emitted due to fossil fuel combustion in PPs. Meeting the GCCs electric power demand on the hottest days, when electric powered air conditioners overwhelm the grid capacity, is real problem. The main benefits of solar air conditioning are lowering carbon emissions, the highest per capita in the world by the GCC, and significantly reduce power grid load. The GCC's abundant and predictable sunshine pattern on one hand, and great difficulties of importing NG to all the GCC, except Qatar, and the continuous need to increase the power plants' capacity make the GCC an ideal candidate to use solar air conditioning.

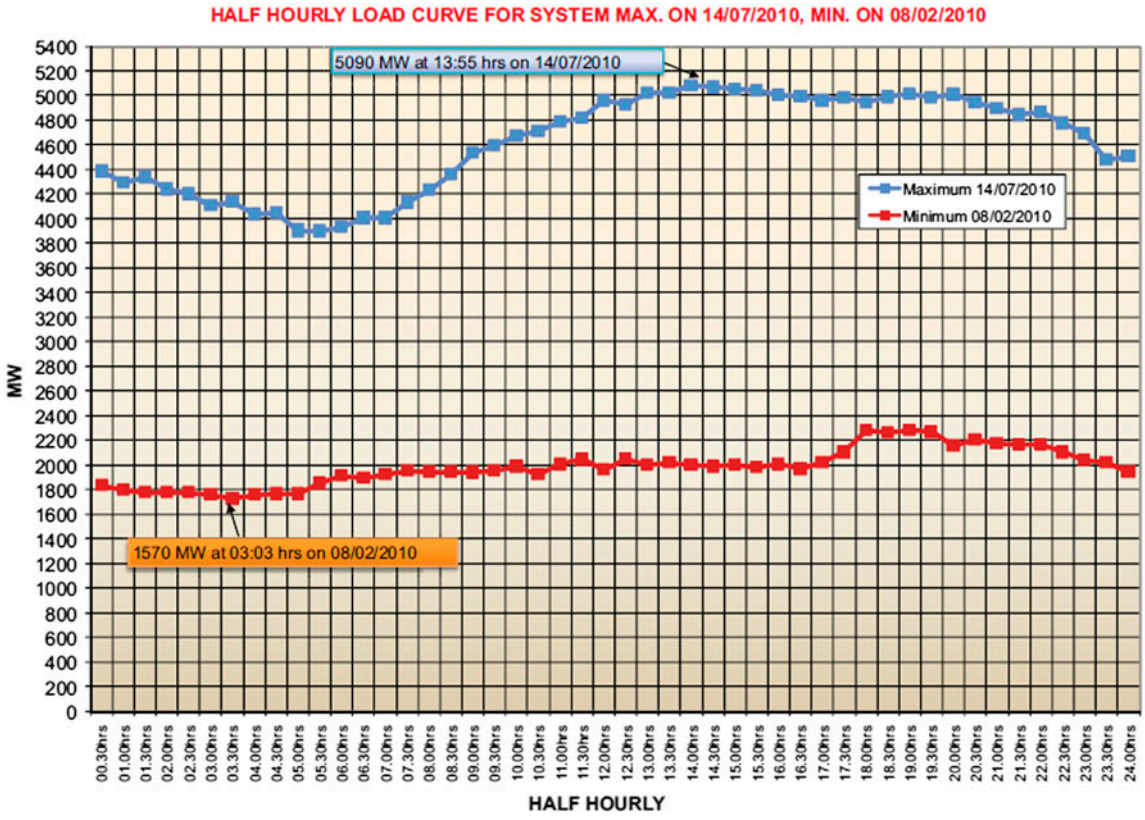

Fig. 3. Qatar EP hourly load variation during the days of maximum load and minimum load in year 2010. [4].

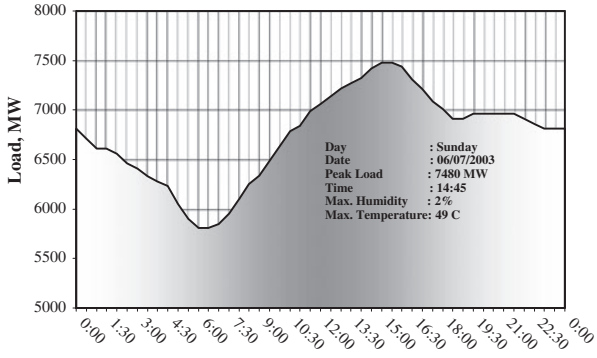

Fig. 4. The peak load on one day in July 2003 in Kuwait, [5].

1.3. Thermal operated cooling system and solar energy

The use of renewable energy resources, different refrigeration cycle, and more friendly refrigerants can reduce the negative environmental impacts of the refrigeration and AC processes. Heat-driven refrigeration cycles are promising solution in this context. Absorption cycles are heat-driven cycles that can use solar energy directly without the need to transform it into electric energy. The other benefit of using heat-driven cycle is the fact that the highest cooling demand is associated with the high solar energy in summer and that offers a good chance for heat-driven cycle to match the cooling demand efficiently.

The temperature of the thermal energy source can affect the selection of the cooling technology as well as the performance of the cycle. Fig. 5 shows the effect of the driving temperature on the coefficient of performance (COP) of different cooling technologies; the COP increases as the driving temperature increases. The driving temperature depends on the solar energy capturing technology that can be adopted and efficiently available. Most of the cooling technologies are working in the range of 80–100˚C, which can be easily achieved using different low-cost solar energy collectors, such as linear Fresnel Collector (LFC) or evacuated tube collectors (ETC).

Two kinds of absorption cycles are commercially available; depending on the refrigerant–absorbent pair; these two cycles are water–lithium bromide (H_2O–LiBr) and ammonia–water (NH_3–H_2O) mixtures. Kurem and Horuz [7] carried out a comprehensive

Table 2
Maximum and minimum EP load from 2006 to 2010 in Qatar, [4]

Year	Maximum load (MW)	Date	Minimum load (MW)	Date
2006	3,230	31-Aug	865	31-Jan
2007	3,550	10-Sep	1,000	1-Jan
2008	3,990	30-Aug	1,115	23-Feb
2009	4,535	24-Aug	1,270	6-Feb
2010	5,090	14-Jul	1,570	8-Feb

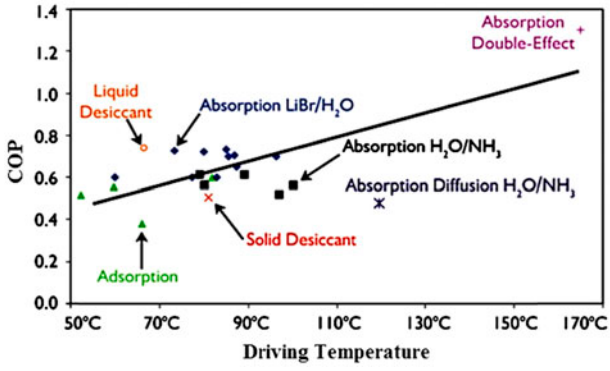

Fig. 5. COP of different cooling cycles as a function of heating medium temperature, [6].

study to investigate and analyze the absorption heat pump (AHP) and absorption heat transformer (AHT) using water–lithium bromide (H_2O–LiBr) and ammonia–water (NH_3–H_2O) mixtures. The authors highlighted and pinpointed the advantages and disadvantages of both the solutions. They concluded that the AHT systems using water–lithium bromide solution produce better COP than that use ammonia–water solution. Cabrera et al. [8] mentioned that the more commonly used systems are the single-effect water–lithium bromide absorption chillers powered by flat-plate or evacuated tube solar collectors. The COP of these chillers are in the range of about 0.5–0.8 at driving temperatures of 75–95˚C, [8]. In this work, a single-effect water–lithium bromide absorption cycle is studied.

Different types of solar thermal energy collectors can be used with single-effect absorption cycles. Cabrera et al. [8] analyzed the use of parabolic trough collectors (PTC) for solar refrigeration and AC applications. They concluded that a modular, small size, and light weight PTC could be easily installed on the rooftop of buildings, and should be target for the manufacturers, [8]. Table 3 compares different types of PTC. Comparison of different cooling systems coupled with PTC is also given in [8], and an overview of the PTC is also given in [9].

Fong et al. [10], compared different cooling technologies and solar collectors for AC applications for buildings in tropical region. They concluded that the PTC has slightly better energy consumption than the flat-plate collectors by 7.3% for the absorption refrigeration, but worse than the ETCs by 36.5%.

Best et al. [11], presented a case study for solar cooling in food industry. In their study, they used a LFC as the optimum collector type because of the working temperatures, performance, cost, and problems in operating conditions related to the studied case (Fig. 6).

They concluded that, for refrigeration application of temperature as low as −2˚C, the LFC is the most convenient collector type. Chemisana et al. [12] also recommended Fresnel reflective solar concentrating system, to be integrated on the building façade, and coupled to a double-effect absorption chiller for space cooling for buildings.

On the other hand, solar desalination technology has been used for long time. Solar energy can be used for seawater desalination either by producing the thermal energy required to drive the thermal energy operated processes or by producing the electric energy required to drive the membrane processes, [13]. The thermal processes include: (a) multistage flash (MSF), (b) multi-effect distillation (MED), (c) solar still, (d) humidification-dehumidification, and (e) membrane distillation (MD). The membrane desalination process includes: (a) reverse osmosis (RO) and (b) electrodialysis (ED). RO system is the most commonly used technology with the lowest specific energy consumption, [14]; nevertheless, it requires extensive pretreatment process and skilled workers. If waste thermal energy is available, it can be directly used to drive a phase-change process such as MSF or MED. The ME plants are more flexible to operate at partial load, less sensible to scaling, cheaper, and more suitable for limited capacity than MSF plants, [14]. The suggested process in this work is MED.

Combining multiple-effect desalination system with different types of absorption cycle heat pumps was investigated by several researchers, [15–21]. The main

Table 3
Overview of different PTC available in the market, [8]

Manufacturer	Model	Type	Aperture width [m]	Weight [kg/m^2]	Conc. ratio C [-]	Tracking mode
Abengoa Solar	PT-1	PTC	2.3	n/a	14	1-axis
	RMT	PTC	1.1	7.7	14	1-axis
Absolicon Solar Concentrator	Absolicon MT 10	PTC	1.1	28.9	n/a	1-axis
	Absolicon T 10	PTC	1.1	28.9	n/a	1-axis
	Absolicon X10 PVT	PTC-PVT	1.1	28.9	n/a	1-axis
Cogenra Solar	SunDeck PVT	PLFR-PVT	1.4	49.4	n/a	1-axis
Composites y Sol	CAPSOL	PTC	1	n/a	18	1-axis
DezhouMingnuo New Energy	PT-3E	PTC	3.0	n/a	14	1-axis
Dr. Vetter	IT. collect	PTC	0.5	14.5	n/a	1-axis
Huayuan New Energy Project	HY-TroughII20–2	PTC	2	n/a	13	1-axis
	HY-TroughII30–2	PTC	3	n/a	19	1-axis
	HY-TroughIII20–2	PTC	2	n/a	9	1-axis
	HY-TroughIII30–2	PTC	3	n/a	14	1-axis
IMK	CSP-trough	PTC	2	n/a	n/a	1-axis
Koluacik Research & Development	SPT-0312	PTC	1.2	47.2	8	2-axis
	SPT-0324	PTC	2.4	33.8	15	2-axis
	SPT-0424	PTC	2.4	29.2	15	2-axis
	SPT-0524	PTC	2.4	32.3	15	2-axis
	SPT-0536	PTC	3.6	27.1	23	2-axis
NEP Solar	Polytrough 1,200	PTC	1.2	25.3	14	1-axis
	Polytrough 1,800	PTC	1.8	17.9	17	1-axis
SMIRRO	Smirro 300	PTC	1.1	14.6	10	1-axis
Solargenix Energy Headquarter	Power Roof	PTC	3.6	n/a	27	1-axis
Solarlite	SL 2300	PTC	2.3	2	n/a	1-axis
Solitem	PTC 1100	PTC	1.1	14.5	n/a	1-axis
	PTC 1800	PTC	1.8	14.2	15	1-axis
	PTC 3000	PTC	3	14	n/a	1-axis
Soltigua	PTMx	PTC	2.4	n/a	n/a	1-axis
Sopogy	SopoHelios	PTC	2.1	10.4	21	1-axis
	SopoNova	PTC	1.7	13.1	21	1-axis
	SopoTitan	PTC	3	n/a	n/a	1-axis
Thermax	SolPac P60	PTC	n/a	n/a	n/a	1-axis
Trivellienergia	SolarWing Evolution	PTC	1.3	18	n/a	1-axis
Hitachi Plant Technologies	Prototype	PTC	n/a	n/a	n/a	1-axis

objective is to improve the performance of the desalination system. However, fewer researches are aimed to co-production of desalinated water and cooling effect. A proposed arrangement of a combined absorption cycle and multi-effect desalination system driven by solar energy was analyzed by Aly, [15]. In his study, the condenser and evaporator of the absorption cycle were replaced by a 20-effects desalination system. The vapor generated in the absorption cycle is used as the heating steam for the desalination system, and dumped out of the cycle for health reasons. The desalination system's top brine temperature (TBT) was 63˚C, while the last effect temperature was 6˚C. For this reason, the vapor generated in this effect is directed to the absorber of the absorption cycle. The system produced 1.53 MGD of fresh water at a GOR of 14.8 and a PR of 14.2. The system can also provide as a byproduct cooling capacity for air conditioning purposes equivalent to a 220 kW vapor compression refrigerating machine. Mandani et al. [16] proposed a

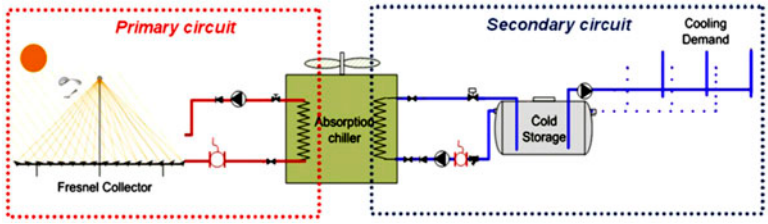

Fig. 6. Solar cooling system using LFC, [11].

connection of a single-effect desalination system with a lithium-bromide heat pump to improve the performance of the desalination system. Their analysis showed a 50–70% improvement of the thermal performance ratios of the system compared with the single-effect thermal vapor compression system.

Alarcón-Padilla et al. [17,18] evaluated the connection of a double-effect AHP driven by a fire-tube gas boiler, to 14 effects MED unit. The hot cooling water from the absorption cycle condenser is used to drive the MED unit. The lower effects are cooled by the cold water produced in the absorption cycle evaporator. They used two water tanks for steady-state operation of the unit. No cooling effect was used in this cycle.

Wang and Lior [19–21], proposed and mathematically analyzed a process of absorption cycle for space cooling combined with a multiple-effect evaporation system for desalination. In their study, the condenser of the absorption cycle is replaced by a low temperature multi-effect evaporation system driven by steam generated in the generator. The system is driven by steam generated externally. The combined system gives a 60–78% water production gain over a stand-alone low-temperature multi-effect evaporation (LT-MEE) unit run by the same heat source conditions.

2. Process description

The proposed system, Fig. 7, consists of three subsystems, namely: (i) the absorption cycle, (ii) the desalination process, and (iii) the solar field. The vapor absorption system consists of an absorber, a generator, a condenser, an evaporator, expansion valves, a solution heat exchanger, and a solution pump as illustrated in Fig. 8. The energy required to drive the absorption system is supplied as thermal energy to the generator. However, a small amount of mechanical work is required to drive the solution pump. This is in contrast to conventional vapor-compression cycle, which mainly requires shaft work for the compression process, [22]. In the evaporator, low-pressure liquid–vapor mixture refrigerant, state 4 in Fig. 8, evaporates on the outer surface of the evaporator's tube bundle.

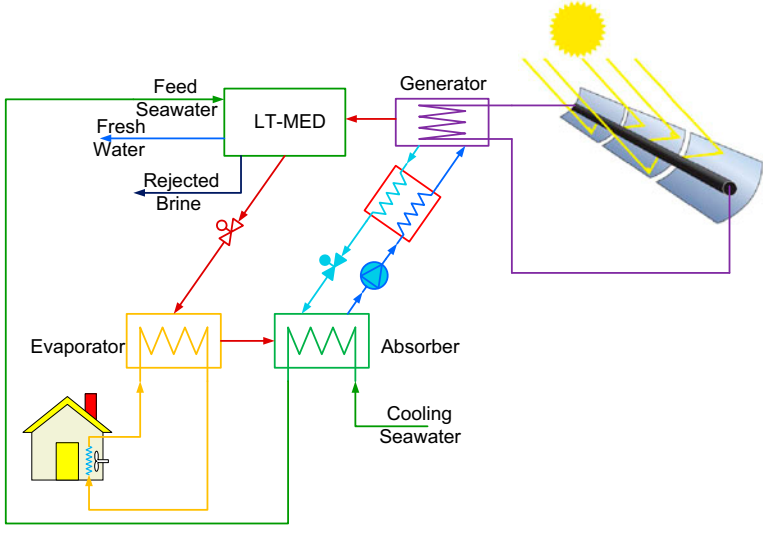

Fig. 7. Block diagram for the proposed system.

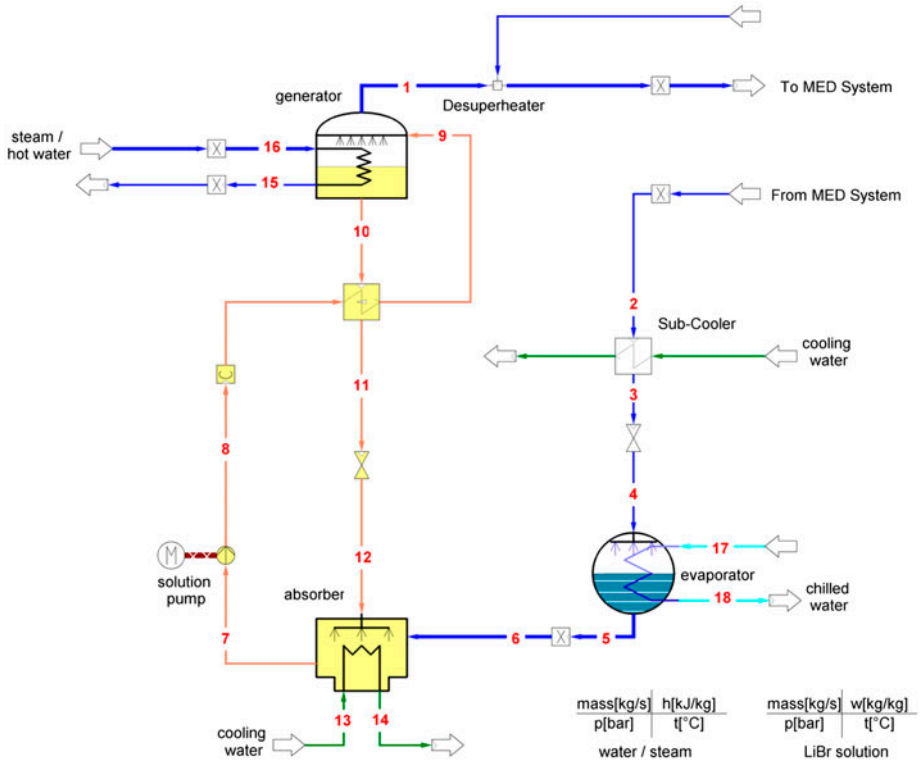

Fig. 8. Schematic diagram of the H_2O–LiBr absorption system.

Heat is supplied to the evaporator by water flowing inside the evaporator's tubes; this chilled water is subsequently used for refrigeration. Refrigerant vapor leaving the evaporator as saturated vapor enters the absorber at low-temperature and low-pressure conditions, state 5. The refrigerant vapor is then absorbed and dissolved by the weak water–lithium bromide (H_2O–LiBr) solution coming from the generator through line 12. It is worth to mention that the weak solution is the solution with less amount of refrigerant, i.e. highly concentrated by LiBr salt. Heat liberated during the absorption process is removed by using cooling water flowing inside the tubes, states 13 and 14. The solution pump receives strong H_2O–LiBr solution through line 7 and delivers it at high pressure to the generator via the solution heat exchanger through line 8. Note that the solution is a saturated liquid and hence the pump work is very small. The high-pressure solution entering the generator through line 9 is heated and the water in the solution is vaporized. The heat for this process could be provided by solar energy or a gas burner. The remaining weak H_2O–LiBr solution exits through line 10 via the heat exchanger to the absorber through a pressure-reducing valve between lines 11 and 12. A solution heat exchanger is included here; as the solution in line 8 requires heating and the hot solution in line 10 would increase the absorber temperature if it were not cooled before entry, [22]. High-pressure, high-temperature refrigerant vapor leaving the generator is passed to the desalination system through line 1. A de-superheater is used before introducing this vapor as heat source in the desalination system. The saturated vapor is condensed to a liquid in the first effect of the MED desalination system. This liquid, then flows through a sub-cooler heat exchanger to reduce its temperature even more to improve the cooling performance of the absorption cycle. The sub-cooled water is then flowed through an expansion valve in line 3 and into the evaporator through line 4.

The proposed thermal desalination system is a low-temperature multi-effect distillation (LT-MED) system. A schematic diagram of the combined system with various significant components is shown in Fig. 9. Based on the mathematical model of the absorption cycle, the amount and conditions of the available driving steam for the desalination system can be accurately estimated. The desalination system can be operated in two modes; (a) conventional LT-MED driven by steam (or hot water) with the

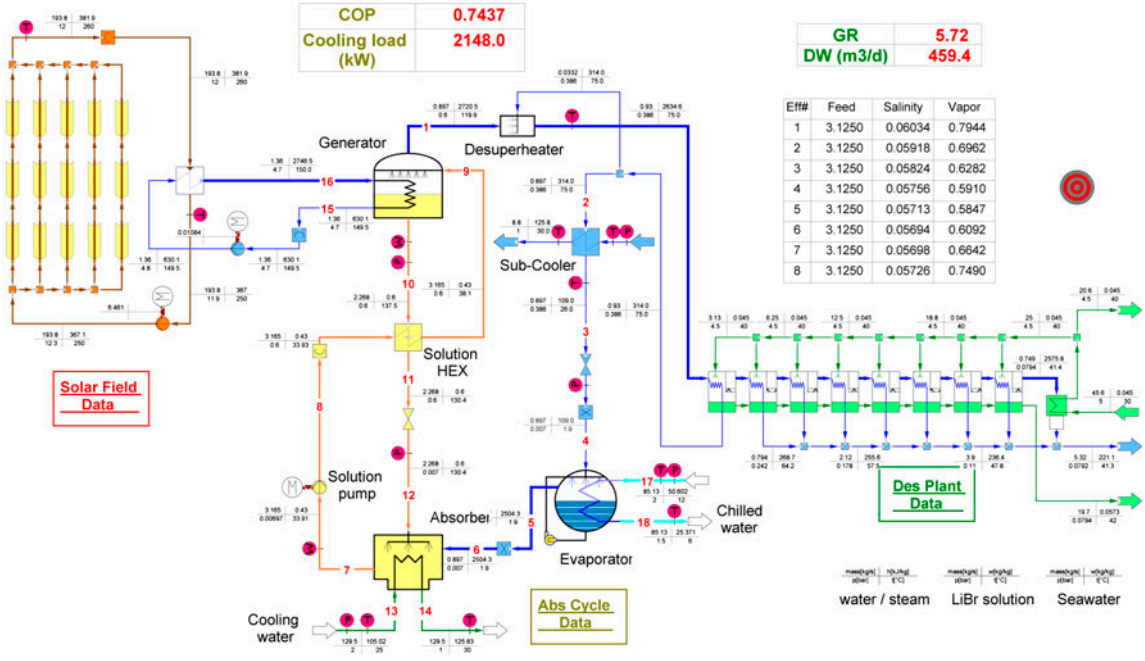

Fig. 9. A schematic diagram for the proposed combined system.

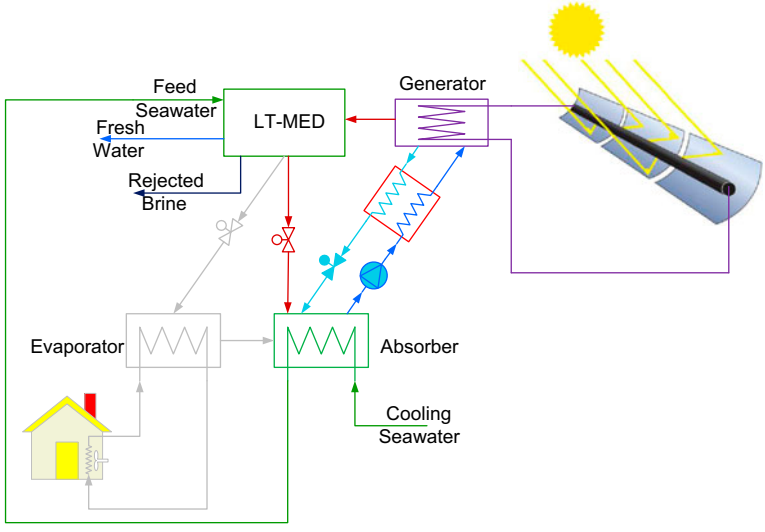

Fig. 10. Layout of the heat pump-assisted desalination system.

lower condenser cooled by the atmospheric seawater, Fig. 7, and (b) a LT-MED system with its lower condenser is connected to the absorber of the absorption cycle, Fig. 10. In the present work, the system operated in the conventional mode will be considered only. A rigorous mathematical model for the desalination process has been developed to design and to predict the performance of the system and to estimate the size of the system components.

3. Mathematical model

3.1. Mathematical model of the MED system

The proposed desalination system arrangement is MED with parallel-cross feed, Fig. 11. The schematic representation of the evaporator is shown in Fig. 12. The following assumptions are considered in the developed mathematical model of the absorption and desalination systems.

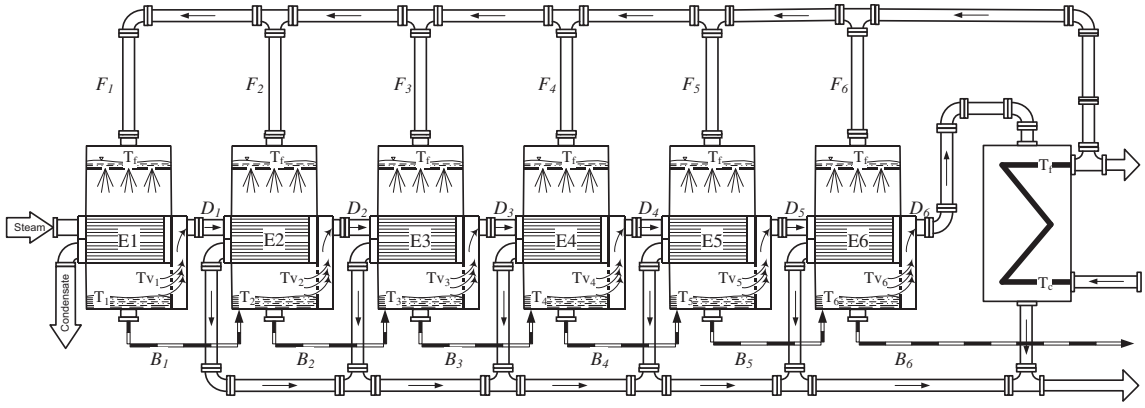

Fig. 11. Parallel-cross feed MED system diagram.

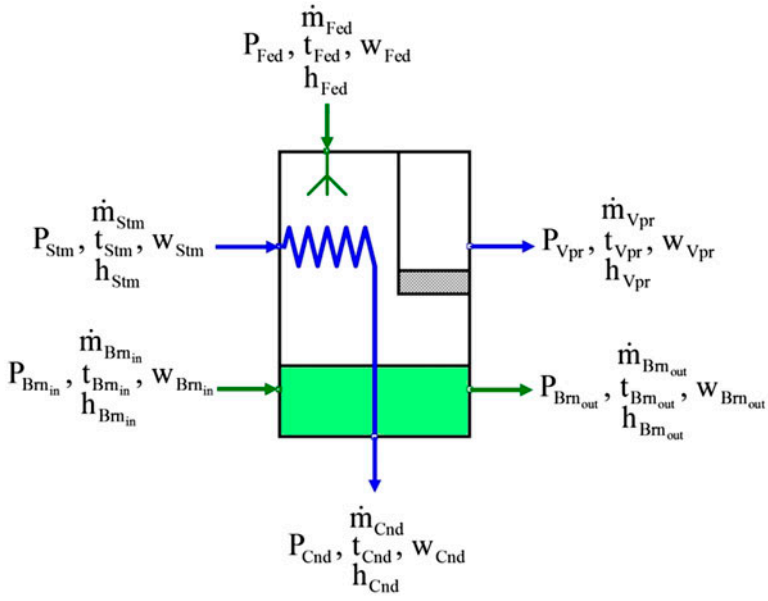

Fig. 12. Schematic diagram of the evaporator modeling variables.

(1) The system runs in a steady-state condition.
(2) Heat losses to the surroundings are neglected.

3.1.1. Material balance through the evaporator

3.1.1.1. Mass conservation of water and steam.

$$\dot{m}_{\mathrm{Fed}} + \dot{m}_{\mathrm{Brn_{in}}} = \dot{m}_{\mathrm{Brn_{out}}} + \dot{m}_{\mathrm{Vpr}} \tag{1}$$

$$\dot{m}_{\mathrm{Stm}} = \dot{m}_{\mathrm{Cnd}} \tag{2}$$

3.1.1.2. Mass conservation of salt.

$$\dot{m}_{\mathrm{Fed}} \times w_{\mathrm{Fed}} + \dot{m}_{\mathrm{Brn_{in}}} \times w_{\mathrm{Brn_{in}}} = \dot{m}_{\mathrm{Brn_{out}}} \times w_{\mathrm{Brn_{out}}} \tag{3}$$

3.1.2. Energy balance of the evaporator

Energy supplied by the condensing steam entering the evaporator (i) from the preceded one ($i-1$) is

$$\dot{Q} = \dot{m}_{\mathrm{Stm}}(h_{\mathrm{Stm}} - h_{\mathrm{Cnd}}) \tag{4}$$

This amount of energy will be utilized to increase the temperature of the feed T_f to the boiling temperature in the effect, T_{b_i}, and to evaporate $\dot{m}_{\text{boiling}}$ of water vapor by boiling

$$\dot{Q} = \dot{m}_{\text{Fed}}(h_{\text{Brn}_{\text{out}}} - h_{\text{Fed}}) + \dot{m}_{\text{boiling}} \times L_v \tag{5}$$

The brine from the preceding effect of a temperature $T_{b_{i-1}} > T_{b_i}$ will boil spontaneously, producing an amount of vapor by flashing to reduce its temperature to reach equilibrium with the brine in this effect. The amount of the generated vapor by flashing can be calculated using the following equation.

$$\dot{m}_{\text{flashing}} \times L_v = \dot{m}_{\text{Brn}_{\text{in}}}(\text{h}_{\text{Brn}_{\text{in}}} - \text{h}_{\text{Brn}_{\text{out}}}) \tag{6}$$

The total amount of the vapor generated in this effect is the sum of the vapor generated by both boiling and flashing

$$\dot{m}_{\text{Vpr}} = \dot{m}_{\text{boiling}} + \dot{m}_{\text{flashing}} \tag{7}$$

The formulae for evaluating the enthalpy and latent heat of vaporization is presented in Appendix A

3.1.3. Heat transfer

The energy supplied to the effect in the form of water vapor, generated in the previous effect, is transferred to the feed seawater from the tube bundle. The estimation of the overall heat transfer coefficient for this process is presented here. The amount of heat transferred to the feed can be calculated using the following equation

$$\dot{Q} = A_{\text{surface}} \times U_o \times \Delta T_{\text{LMTD}} \tag{8}$$

where A_{surface} is the total heat transfer area of the tube bundle, U_0 is the overall heat transfer coefficient, and ΔT_{LMTD} is the driving temperature diffidence between the vapor flowing inside the tubes and the feed flow over the outer surface of the tubes. The steam flows inside the tube bundle as a saturated vapor at a temperature T_s of the previous effect which is higher than the boiling temperature T_b in the effect, and leave as condensate at a temperature T_c. The feed, at a temperature T_f, is sprayed on the outer surface of the tube bundle, and its temperature starts to increase to reach T_b. As the temperature of the feed increases from T_f to T_b, the driving temperature difference is decreasing and hence the logarithmic mean temperature difference is used in this model. Fig. 13 represents the temperature profiles in the effect.

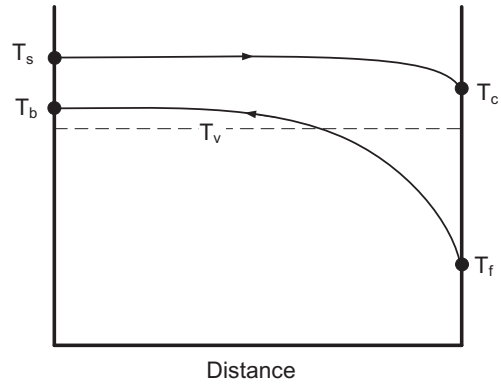

Fig. 13. Temperature profiles in the effect.

According to the temperature profile shown in Fig. 13, the log mean temperature difference in this case is

$$\Delta T_{\text{LMTD}} = \frac{(T_s - T_b) - (T_c - T_f)}{\ln \frac{(T_s - T_b)}{(T_c - T_f)}} \tag{9}$$

In case of sub-cooling, the condensate temperature is $T_c < T_s$ by the sub-cooling temperature difference, ΔT_{sub}, where

$$\Delta T_{\text{sub}} = T_s - T_c \tag{10}$$

The vapor generated in this effect is considered the supply steam for the next effect. The generated vapor temperature is T_v less than the brine temperature by the boiling point elevation T_{BPE} as follows

$$T_v = T_b - T_{\text{BPE}} \tag{11}$$

The formula for estimating T_{BPE} is presented in Appendix A.

The overall heat transfer coefficient U_0 based on the outside surface of the tube is defined as:

$$\frac{1}{U_o} = \left(\frac{d_o}{h_i d_i}\right) + \left(R_{f,i}\frac{d_o}{d_i}\right) + \left(\frac{d_o}{2k_{\text{tube}}}\right) \ln\left(\frac{d_o}{d_i}\right) + R_{f,o} + \left(\frac{1}{h_o}\right) \tag{12}$$

In the evaporators, the feed water is boiling and evaporated on the outer surface of the tube in the form of thin film boiling, while inside the tubes, the steam is condensed. In the condenser, the vapor condenses on the outer surface of the tube, while the water inside the tube is heated. For each case, a suitable formula is used to estimate the heat transfer coefficient and then substitute into Eq. (12).

3.1.3.1. Heat transfer in evaporator. The heat transfer coefficient of boiling thin film over the outer surface of the evaporator's tube bundle, h_0, was developed by Han and Fletcher [23], and used by many researchers, [24–29].

$$\bar{h}_o\left(\frac{\mu^2}{\rho^2 g k^3}\right)^{1/3} = 0.0004\ \mathrm{Re}^{0.2}\mathrm{Pr}^{0.65}q''^{0.4}$$
$$\text{where}\quad q'' = \frac{q}{\pi dLN};\ \mathrm{Re} = \frac{4\dot{m}}{2L\mu\sqrt{N}} \tag{13}$$

Heat transfer coefficient of thin film condensation inside evaporator's tube, Fig. 14, can be evaluated using the correlation developed by Shah [30] below. The developed correlation based on linear variation of the vapor quality along the heat exchanger length, the average heat transfer coefficient along the evaporator can be evaluated using Eq. (14).

$$\bar{h}_i = h_\ell\left(0.55 + \frac{2.09}{\mathrm{Pr}_\ell^{0.38}}\right)$$
$$\text{where}\quad h_\ell = 0.023\,(\mathrm{Re}_\ell)^{0.8}\,(\mathrm{Pr}_\ell)^{0.4}\left(\frac{k_\ell}{D}\right) \tag{14}$$

3.1.3.2. Heat transfer in end condenser. Condensation of vapor over the outer surface of tube bundle has different modes, Fig. 15. The heat transfer coefficient of the water vapor in the condenser can be evaluated using Eq. (15), [31].

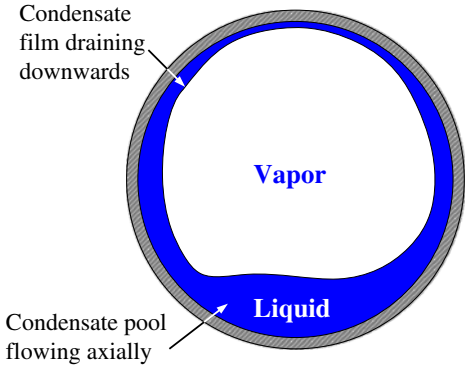

Fig. 14. Film condensation inside evaporator tube.

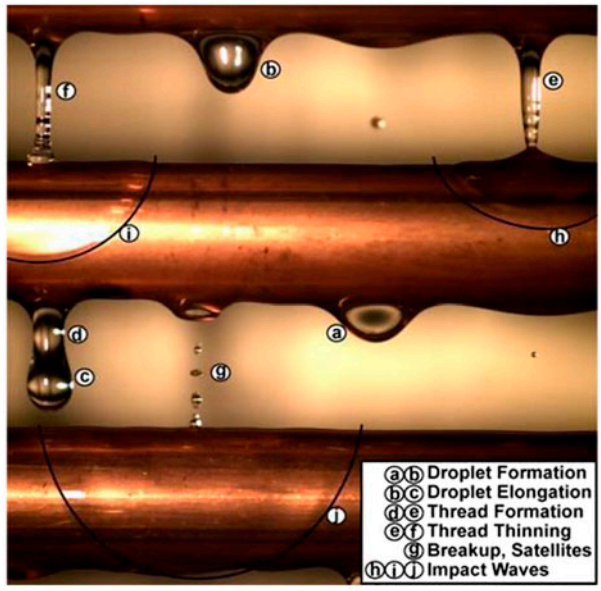

Fig. 15. Different condensation mode over tube bundle, [32].

$$h_o = 0.729\left[\frac{g\,\rho_l(\rho_l - \rho_v)k_l^3\,h'_{fg}}{N_c\,\mu_l\,D\,(T_{\mathrm{sat}} - T_w)}\right]^{1/4}$$
$$\text{where}\quad h'_{fg} = h_{fg} + 0.68\,C_{p,l}(T_{\mathrm{sat}} - T_w) \tag{15}$$

For the turbulent flow of water in a pipe, e.g. cooling water of the condenser, Gnielinski correlation [33] is used, Eq. (16). This correlation was based on a comprehensive review of many correlations for turbulent flow through tubes and was recommended by [34–36].

$$\overline{\mathrm{Nu}} = \frac{(f/8)(\mathrm{Re}_D - 1,000)\,\mathrm{Pr}}{1 + 12.7(f/8)^{1/2}\left(\mathrm{Pr}^{2/3} - 1\right)}\left[1 + (D/L)^{2/3}\right]$$
$$\text{for } 0.5 < \mathrm{Pr} < 2000 \quad \text{and} \quad 2,300 < \mathrm{Re}_D < 5 \times 10^6 \tag{16}$$

The D/L factor in Eq. (16) accounts for entrance effects. For fully developed flow, D/L = 0.0. The friction factor f is defined for a fully developed turbulent flow in an aerodynamically smooth duct as [34,37]:

$$f = \frac{1}{(0.79\ \ln\ \mathrm{Re}_D - 1.64)^2} \quad \text{for } 3000 < \mathrm{Re}_D < 5.0 \times 10^6 \tag{17}$$

3.2. Mathematical model of the absorption cycle

A schematic diagram of a single-effect H_2O–LiBr absorption system is shown in Fig. 8. The schematic diagram shows the main component of the proposed cycle, where the condenser is replaced by the first effect of the distillation system (not shown in this diagram). In this diagram, a sub-cooler heat exchanger is added to the cycle to reduce the temperature of the condensate of the MED system to improve the cooling capacity of the absorption cycle. In addition, a de-superheater is added after the generator to ensure saturated vapor is supplied to the MED system.

Model assumptions

(1) Refrigerant leaving the evaporator is saturated water vapor.
(2) Refrigerant leaving the condenser is saturated liquid water.
(3) No liquid carry over from evaporator.
(4) Refrigerant vapor leaving the generator has the equilibrium temperatures of the weak solution of the generator's pressure and is salt free.
(5) The solutions leaving the generator and absorber are saturated.
(6) The pumping process is isentropic.

The thermodynamic model of each component is explained in the following section.

3.2.1. Evaporator

In the evaporator, Fig. 16, the low-pressure, low-temperature refrigerant (after the expansion valve) is sprayed over the evaporator tube, where the cold water circulates through the tubes and gets chilled.

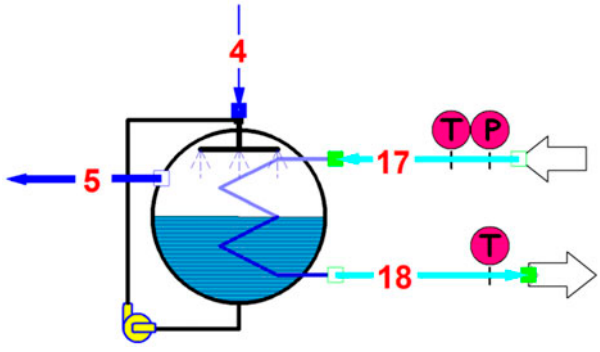

Fig. 16. Evaporator illustration.

3.2.1.1. Mass balances.

$$\dot{m}_4 = \dot{m}_5 \quad \text{and} \quad \dot{m}_{17} = \dot{m}_{18} \tag{18}$$

3.2.1.2. Energy balances.

$$\dot{Q}_{\text{trans}} = \dot{m}_4 \times (h_5 - h_4) \tag{19}$$

$$\dot{Q}_{\text{trans}} = \dot{m}_{17} \times (h_{17} - h_{18}) \tag{20}$$

3.2.1.3. Heat transfer [38].

$$\dot{Q}_{\text{trans}} = (\text{UA})_{\text{evap}} \, (\Delta T_{\text{LMTD}})_{\text{evap}} \tag{21}$$

$$(\Delta T_{\text{LMTD}})_{\text{evap}} = \left(\frac{\delta t_1 - \delta t_2}{\ln(\delta t_1 / \delta t_2)} \right)_{\text{evap}} \tag{22}$$

$$\begin{aligned} \delta t_1 &= t_{17} - t_4 \\ \delta t_2 &= t_{18} - t_5 \end{aligned} \tag{23}$$

3.2.2. Absorber

In the absorber, Fig. 17, the saturated vapor refrigerant is absorbed by the weak solution introduced at state 12 and converted to low pressure strong solution at state 7. The generated heat is removed by the cooling water.

3.2.2.1. Mass balances.

$$\begin{aligned} \dot{m}_{12} + \dot{m}_6 &= \dot{m}_7 \\ \dot{m}_{13} &= \dot{m}_{14} \end{aligned} \tag{24}$$

3.2.2.2. LiBr mass balance.

$$\dot{m}_{12} \times z_{12} = \dot{m}_7 \times z_7 \tag{25}$$

3.2.2.3. Energy balances.

$$\dot{Q}_{\text{trans}} = \dot{m}_6 h_6 + \dot{m}_{12} h_{12} - \dot{m}_7 h_7 \tag{26}$$

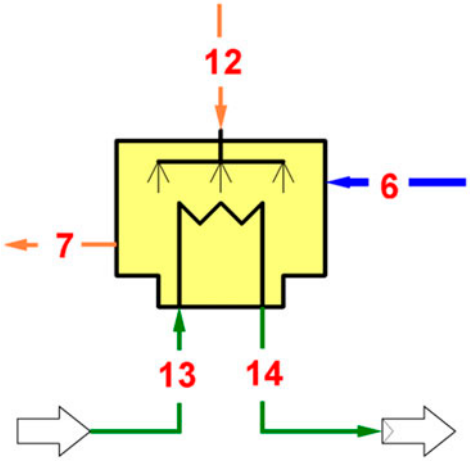

Fig. 17. Absorber illustration.

$$\dot{Q}_{\text{trans}} = \dot{m}_{13} \times (h_{14} - h_{13}) \tag{27}$$

3.2.2.4. Heat transfer [38,39].

$$\dot{Q}_{\text{trans}} = (UA)_{\text{abs}} (\Delta T_{\text{LMTD}})_{\text{abs}} \tag{28}$$

$$(\Delta T_{\text{LMTD}})_{\text{abs}} = \left(\frac{\delta t_1 - \delta t_2}{\ln(\delta t_1 / \delta t_2)} \right)_{\text{abs}} \tag{29}$$

$$\begin{aligned} \delta t_1 &= t_{12} - t_{14} \\ \delta t_2 &= t_7 - t_{13} \end{aligned} \tag{30}$$

3.2.3. Generator

The strong solution at state 9 is introduced to the generator, Fig. 18, where heat energy is supplied by hot water or steam. The heat energy separates the refrigerant vapor from the solution and a high LiBr concentrated solution is exits at state 10.

3.2.3.1. Mass balances.

$$\begin{aligned} \dot{m}_9 &= \dot{m}_1 + \dot{m}_{10} \\ \dot{m}_{16} &= \dot{m}_{15} \end{aligned} \tag{31}$$

3.2.3.2. LiBr mass balance.

$$\dot{m}_9 \times z_9 = \dot{m}_{10} \times z_{10} \tag{32}$$

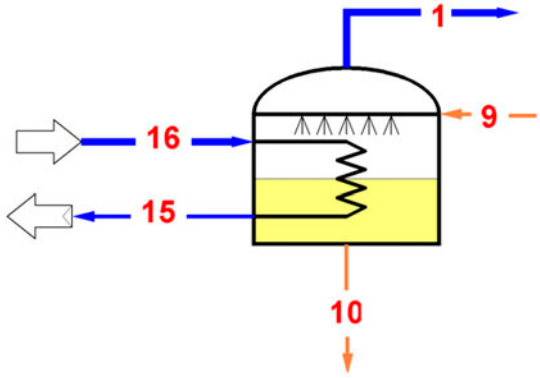

Fig. 18. Generator illustration.

3.2.3.3. Energy balances.

$$\dot{Q}_{\text{trans}} = \dot{m}_1 h_1 + \dot{m}_{10} h_{10} - \dot{m}_9 h_9 \tag{33}$$

$$\dot{Q}_{\text{trans}} = \dot{m}_{16} \times (h_{16} - h_{15}) \tag{34}$$

3.2.3.4. Heat transfer [38].

$$\dot{Q}_{\text{trans}} = (\text{UA})_{\text{gen}} (\Delta T_{\text{LMTD}})_{\text{gen}} \tag{35}$$

$$(\Delta T_{\text{LMTD}})_{\text{gen}} = \left(\frac{\delta t_1 - \delta t_2}{\ln(\delta t_1 / \delta t_2)} \right)_{\text{gen}} \tag{36}$$

$$\begin{aligned} \delta t_1 &= t_{16} - t_9 \\ \delta t_2 &= t_{15} - t_{10} \end{aligned} \tag{37}$$

The values of the design variables in Table 4 will be used in this work.

The equations comprising the mathematical model of the combined system are utilized in IPSEpro software, [41] and the results are presented hereafter.

3.3. Mathematical model of the solar field

A simple solar field model is used to evaluate the amount of heat gained by the PTC solar field illustrated in Fig. 19. Table 5 shows the monthly average solar irradiance on Doha. The maximum average irradiance is 0.65 kW/m^2 in April and the minimum is 0.44 kW/m^2 in November with the yearly average of 0.55 kW/m^2.

$$Q_{\text{incident}} = I \times A_{\text{aperture}} \tag{38}$$

Table 4
Design values for the absorption cycle, [40]

Heat exchanger	UA, (kW/K)	Conditions
Evaporator	319.2	Countercurrent film
Absorber	186.9	Countercurrent film absorber
Generator	143.4	Pool generator
Solution HEX	33.8	Countercurrent

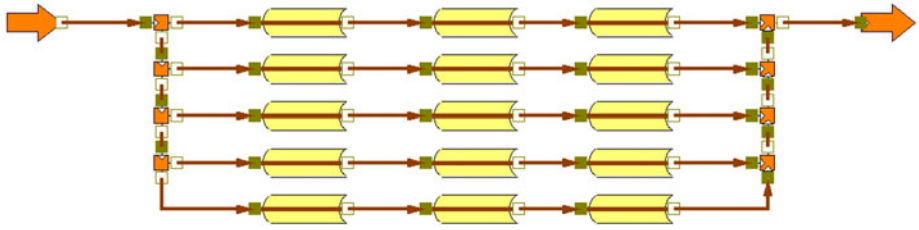

Fig. 19. PTC Solar Field.

Table 5
Monthly average solar irradiance on Doha City

Month	Sunshine hours from [42] (h)	Irradiance from [42] (kW/m^2)	H from [43] (MJ/m^2)	Irradiance calculated from [43] (kW/m^2)	Irradiance avg. calculated (kW/m^2)
Jan	8.0	0.46	13.75	0.48	0.47
Feb	8.1	0.54	16.28	0.56	0.55
Mar	7.8	0.63	18.02	0.64	0.63
Apr	9.0	0.63	21.53	0.66	0.65
May	10.5	0.59	23.39	0.62	0.60
Jun	11.5	0.57	24.32	0.59	0.58
Jul	10.5	0.57	22.83	0.60	0.59
Aug	10.7	0.54	22.51	0.58	0.56
Sep	10.2	0.54	20.64	0.56	0.55
Oct	9.9	0.48	17.61	0.49	0.49
Nov	9.3	0.44	14.98	0.45	0.44
Dec	7.7	0.45	12.79	0.46	0.46
Avg.	9.4	0.54	19.05	0.56	0.55

where Q_{incident} is the amount of incident solar energy on the PTC, I is the solar irradiance on city of Doha, and A_{aperture} is the aperture area of the solar collector

$$Q_{\text{gain}} = Q_{\text{incident}} \times \eta_C \tag{39}$$

Qgain represents the amount of thermal energy gained by the heat transfer fluid flowing through the PTC where average value of the collector efficiency η_c is used; $\eta_c = 0.7$ is used in the present work.

4. Results and discussion

The proposed system was modeled and simulated using IPSEpro software. The results of the system for cooling load at the absorption cycle of 1,500 kW and solar irradiance of 0.65 kw/m^2 are shown in the following tables. Table 6 shows result's summary of the absorption cycle.

Table 7 shows the results summary of the MED desalination system. The TBT is assumed to be 65 ℃.

Table 8 shows the summary of the solar field results. The average value of the collector efficiency is assumed to be 0.7, while the maximum solar irradiance on Doha is 0.65 kW/m^2

The solar irradiance values in Table 5 were used to estimate the solar field area and collectors' length as illustrated in Fig. 20. Maximum required collector's area to produce 1,500 kW of the cooling load was

Table 6
Absorption cycle results

	Parameter	Units	Value
1	Cooling load	kW	1,500
2	COP	–	0.88
3	Evaporator temperature	°C	1.87
4	Evaporator pressure	bar	0.007
5	Refrigerant flow rate	kg/s	0.631
6	Chilled water flow rate	kg/s	89.1
7	Chilled water temperature	°C	6
8	Warm water temperature	°C	10
9	Chilled water temperature drop	°C	4
10	Condenser heat transfer	kW	1636.3
11	Condenser temperature	°C	30
12	Generator heat transfer	kW	1692.2
13	Generator temperature	°C	137.5
14	Absorber heat transfer	kW	1556.1
15	Absorber temperature	°C	65.84
16	Concentrated solution flow rate	kg/s	1.6
17	Diluted solution flow rate	kg/s	2.23
18	High LiBr concentration	-	0.6
19	Low LiBr concentration	-	0.43
20	High temperature of the heating steam	°C	150
21	Low temperature of the heating steam	°C	149.5
22	Solution pump power	kW	0.183
23	Supply steam flow rate	kg/s	0.8
24	Total energy input to the cycle	kW	1692.4

Table 7
Desalination plant results

	Parameter	Units	Value
1	GR	–	5.69
2	Distillate flow rate	kg/s	3.72
3	Top brine temp.	°C	65
4	Thermal energy input	kW	1517.5
		kJ/kg	407.93
		kWh/m^3	113.3
5	Steam flow rate	kg/s	0.654
6	Feed flow rate	kg/s	32.0
7	Brine flow rate	kg/s	14.14
8	Cooling water flow rate	kg/s	14.13
9	Brine salinity	g/l	56.83

found to be 5,484 m^2 with total collector's length of 1,097 m.

IPSEpro software was used to simulate the combined system. The flow sheet in Fig. 10 illustrates the combined system as represented by the simulation software. The effect of changing cooling load of the absorption cycle on the system performance parameters is shown in Figs. 21–26.

Table 8
Solar field results

	Parameter	Units	Value
1	Total solar field area	m^2	3712.5
2	Total length of the collectors	m	742.5
3	Aperture area of one collector	m^2	247.5
4	Collector width	m	5
5	Total mass flow rate of HTF	kg/s	102.2
6	Hot fluid temperature	°C	261.0
7	Cold fluid temperature	°C	250.0
8	Irradiance	kW/m^2	0.65
9	Collector average efficiency	–	0.7
10	Energy gain	kW	1692.2

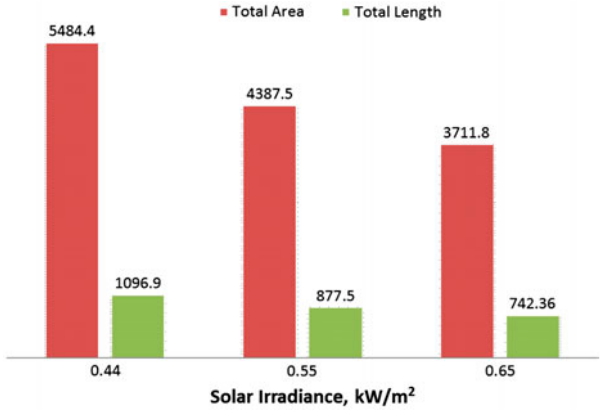

Fig. 20. Solar field area and collectors lengthfor different solar irradiance.

The effect of cooling load on the heat transfer in each heat exchanger of the absorption cycle is illustrated in Fig. 21. As mentioned before, the condenser is replaced by the desalination system; however, the condenser heat transfer is calculated from the states of the refrigerant after the generator and before the expansion valve. As expected, the heat transfer in each heat exchanger is increased with the increase in the cooling load. The total energy supplied to the absorption cycle, the mass flow rate of the refrigerant and the supply steam, and the COP of the cycle are presented in Fig. 22. As the cooling load increases, the required steam supply by the solar field and the LiBr solution flow rate are increased and hence the total energy supply to the cycle increases steeply. The COP of the cycle

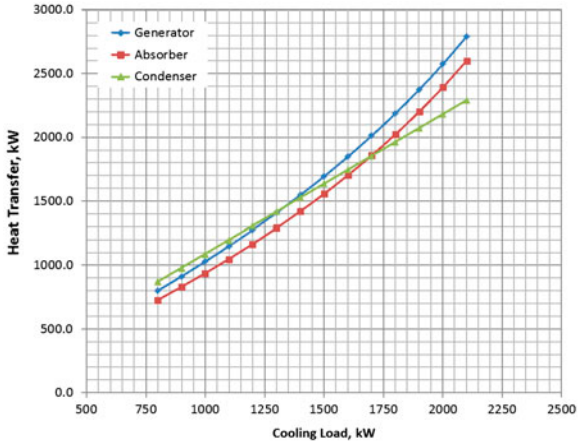

Fig. 21. Heat transfer in the different components of the absorption cycle.

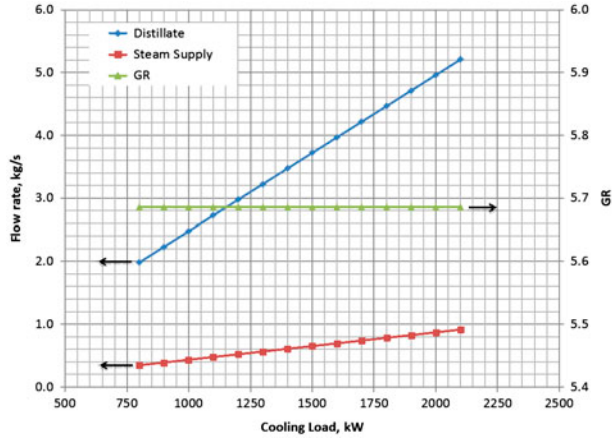

Fig. 23. GR, distillate, and steam supply of the MED desalination system.

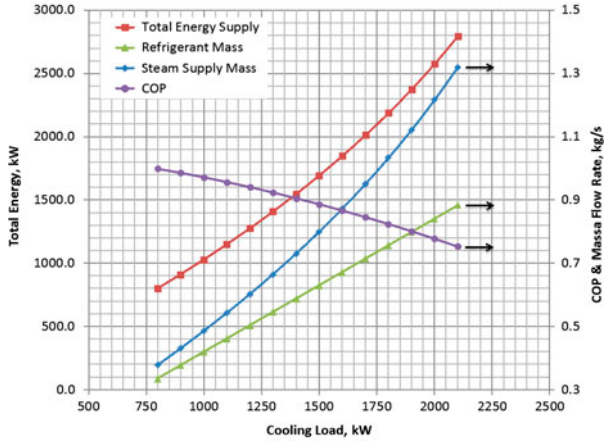

Fig. 22. COP, Energy supply, steam, and refrigerant flow rate as a function of the cooling load.

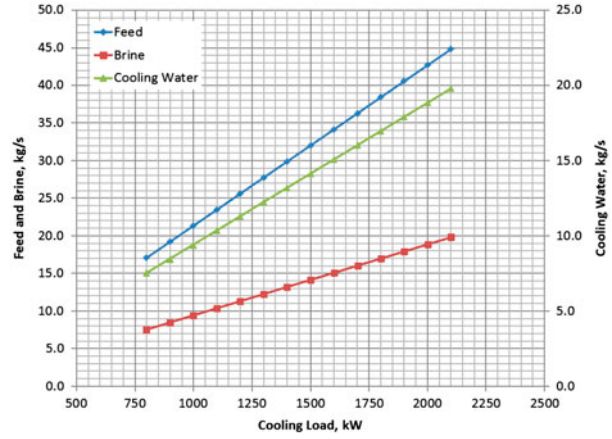

Fig. 24. Different streams flow rate of the MED system.

decreases as shown in Fig. 22 due to the much increase in the steam supply compared with the refrigerant flow rate, the difference between it increases with the increase in the cooling load.

Fig. 23 shows the performance of the MED desalination system as a function of the cooling load of the absorption cycle. The ratio of the distillate produced per kg of the supply steam (GR) was constant as the amount of the feed to the system was controlled by the salinity in the last effect of the desalination system. As the cooling load increases, the refrigerant flow in the absorption cycle increases, as illustrated in Fig. 22, which represents the heating steam supply to the desalination system, which in turns increases the distillate production by the system. The feed flow rate to the MED system was also increased, as shown in Fig. 24, to keep the salinity constant in the last effect, which resulted in a constant GR of the MED system. As shown in Fig. 24, the flow rate of brine and cooling water is also increased as a result to increasing the feed flow rate.

The effect of the cooling load on the solar field parameters are shown in Figs. 25 and 26. The required collector's length and hence the aperture areas increase as the required steam supply by the absorption cycle increases. As a result to the increase in solar field area, the required heat transfer fluid flow is also increased to increase the solar heat gain.

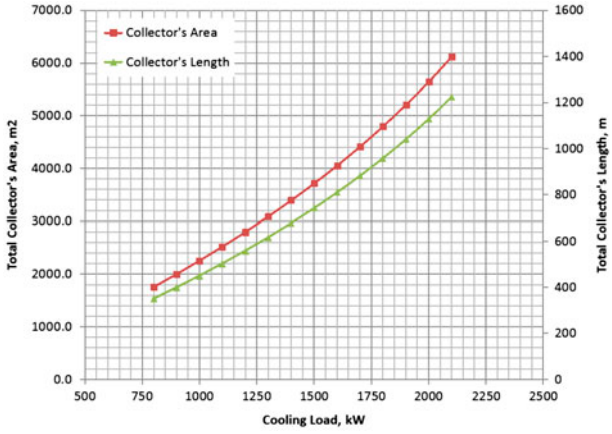

Fig. 25. Total length and total aperture area of the solar field.

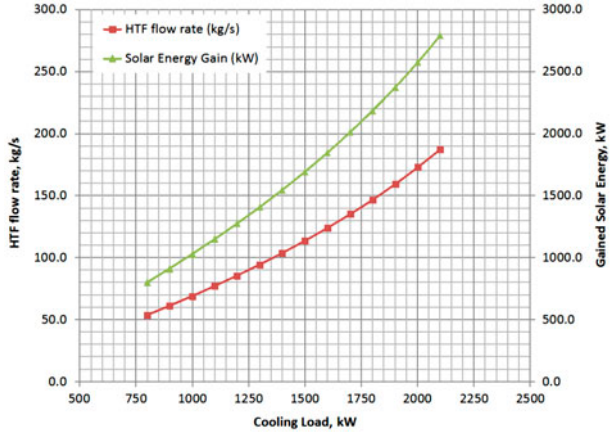

Fig. 26. Heat transfer fluid flow and gained solar energy as a function of the cooling load.

5. Conclusion

A combined system of H_2O–LiBr absorption, refrigeration, and MED-LT desalination system was proposed, modeled, and simulated in this paper. The thermal energy waste of the condenser of the absorption cycle is used to drive the desalination system. A parametric study on the effect of the cooling load of the absorption cycle on the performance of the combined system is carried out and the results are presented. The cooling load affects the amount of produced water but keeps the GR constant at 5.7. In addition, increasing the cooling load increases the required solar field area and the flow rate of the heat transfer fluid.

Nomenclature

Variables

$A_{surface}$	m^2	—	heat transfer surface area
d_i, d_0	m	—	inner and outer diameters
f	–	—	frication coefficient
h	kJ/kg	—	specific enthalpy
h_i, h_0	kW/m^2℃	—	inner and outer convection heat transfer coefficient
k_{tube}	kW/m℃	—	tube thermal conductivity
L	m	—	tube length
L_v	kJ/kg	—	latent heat of the vapor
$\dot{m}$	kg/s	—	mass flow rate
N	–	—	number of tubes
Nu	–	—	Nusselt number
p	bar	—	pressure
Pr	–	—	Prendtl number
$\dot{Q}$	kW	—	heat transfer
Re	–	—	Reynolds number
R_{fi}, R_{f0}	kW/℃	—	inner and outer fouling resistance
t	℃	—	temperature
T_b	℃	—	brine temperature
T_{BPE}	℃	—	boiling point elevation
T_c	℃	—	condensate temperature
T_f	℃	—	feed temperature
T_s	℃	—	steam temperature
T_v	℃	—	vapor temperature
U_0	kW/m^2℃	—	overall heat transfer coefficient
w	–	—	seawater salinity
z	–	—	LiBr concentration

Greek

μ	kg/ms	—	fluid viscosity
ΔT_{LMTD}	℃	—	log mean temperature difference

Subscript

abs	—	absorber
Brn	—	brine
Cnd	—	condensate
evap	—	evaporator
Fed	—	feed
gen	—	generator
sat	—	saturated
Stm	—	steam
trans	—	transfer
Vpr	—	vapor
w	—	wall

References

[1] R. Kombargi, O. Waterlander, G. Sarraf, A. Sastry, Gas shortage in the GCC how to bridge the gap. Available from: http://www.booz.com/media/uploads/Gas_Shortage_in_the_GCC.pdf (accessed 20 February 2014).

[2] Countries—U.S. Energy Information Administration (EIA). [Online]. Available from: http://www.eia.gov/countries/ (accessed 20 February 2014).
[3] Heating, ventilation, and air conditioning (HVAC) market in the GCC, July 2012. [Online]. Available from: http://www.constructarabia.com/wp-content/uploads/downloads/2012/07/GCC-HVACMarket-2012.pdf (accessed 15 January 2014).
[4] Qatar general electricity and water Corporation (KAHRAMAA), Statistical Report, 2010, 2010. [Online]. Available from: www.km.com.qa (accessed 15 January 2014).
[5] M. Darwish, H. Abdulrahim, A.B. Amer, On better utilization of gas turbines in Kuwait, Energy 33 (2008) 571–588.
[6] C. Balaras, G. Grossman, H.M. Henning, C.A. Infante Ferreira, E. Podesser, L. Wang, E. Wiemken, Solar air conditioning in Europe—An overview, Renewable Sustainable Energy Rev. 11(2) (2007) 299–314.
[7] E. Kurem, I. Horuz, A comparison between ammonia-water and water-lithium bromide solutions in absorption heat transformers, Int. Commun. Heat Mass Transfer 28(3) (2001) 427–438.
[8] F.J. Cabrera, A. Fernández-García, R.M.P. Silva, M. Pérez-García, Use of parabolic trough solar collectors for solar refrigeration and air-conditioning applications, Renewable Sustainable Energy Rev. 20 (April 2013) 103–118.
[9] A. Fernández-García, E. Zarza, L. Valenzuela, M. Pérez, Parabolic-trough solar collectors and their applications, Renewable Sustainable Energy Rev. 14(7) (September 2010) 1695–1721.
[10] K.F. Fong, T.T. Chow, C.K. Lee, Z. Lin, L.S. Chan, Comparative study of different solar cooling systems for buildings in subtropical city, Sol. Energy 84(2) (February 2010) 227–244.
[11] R. Best, J.M. Aceves, H. Islas, F.L. Manzini, I. Pilatowsky, R. Scoccia, M. Motta, Solar cooling in the food industry in Mexico: A case study, Appl. Therm. Eng. 50(2) (February 2013) 1447–1452.
[12] D. Chemisana, J. López-Villada, A. Coronas, J.I. Rosell, C. Lodi, Building integration of concentrating systems for solar cooling applications, Appl. Therm. Eng. 50 (2) (February 2013) 1472–1479.
[13] S. Kalogirou, Survey of solar desalination systems and system selection, Energy 22(1) (1997) 69–81.
[14] L. García-Rodríguez, Renewable energy applications in desalination: State of the art, Sol. Energy 75(5) (November 2003) 381–393.
[15] S.E. Aly, A study of a new thermal vapor compression/multi-effect stack (TVC/MES) low temperature distillation system, Desalination 103(3) (December 1995) 257–263.
[16] F. Mandani, H. Ettouney, H.T. El-Dessouky, LiBr-H2O absorption heat pump for single-effect evaporation desalination process, Desalination 128 (2000) 161–176.
[17] D.C. Alarcón-Padilla, L. García-Rodríguez, J. Blanco-Gálvez, Experimental assessment of connection of an absorption heat pump to a multi-effect distillation unit, Desalination 250(2) (2010) 500–505.
[18] D.C. Alarcón-Padilla, L. García-Rodríguez, J. Blanco-Gálvez, Design recommendations for a multi-effect distillation plant connected to a double-effect absorption heat pump: A solar desalination case study, Desalination 262(1–3) (November 2010) 11–14.
[19] Y. Wang, N. Lior, Thermoeconomic analysis of a low-temperature multi-effect thermal desalination system coupled with an absorption heat pump, Energy 36(6) (June 2011) 3878–3887.
[20] Y. Wang, N. Lior, Proposal and analysis of a high-efficiency combined desalination and refrigeration system based on the LiBr-H_2O absorption cycle-Part 1: System configuration and mathematical model, Energy Convers. Manage. 52 (2011) 220–227.
[21] Y. Wang, N. Lior, Proposal and analysis of a high-efficiency combined desalination and refrigeration system based on the LiBr-H_2O absorption cycle-Part 2: Thermal performance analysis and discussions, Energy Convers. Manage. 52 (2011) 228–235.
[22] M. Nguyen, S. Riffat, D. Whitman, Solar/gas-driven absorption heat-pump systems, Appl. Therm. Eng. 16 (4) (1996) 347–356.
[23] J.-C. Han, L.S. Fletcher, Falling film evaporation and boiling in circumferential and axial grooves on horizontal tubes, Ind. Eng. Chem. Process Des. Dev. 24(3) (July 1985) 570–575.
[24] M.W. Shahzad, A. Myat, W.G. Chun, K.C. Ng, Bubble-assisted film evaporation correlation for saline water at sub-atmospheric pressures in horizontal-tube evaporator, Appl. Therm. Eng. 50(1) (January 2013) 670–676.
[25] M. Ameri, S.S. Mohammadi, M. Hosseini, M. Seifi, Effect of design parameters on multi-effect desalination system specifications, Desalination 245(1–3) (September 2009) 266–283.
[26] H. Ettouney, Design of single-effect mechanical vapor compression, Desalination 190(1–3) (April 2006) 1–15.
[27] J. Uche, J. Artal, L. Serra, Comparison of heat transfer coefficient correlations for thermal desalination units, Desalination 152 (2003) 195–200.
[28] H.T. El-Dessouky, H. Ettouney, F. Mandani, Performance of parallel feed multiple effect evaporation system for seawater desalination, Appl. Therm. Eng. 20 (2000) 1679–1706.
[29] H.T. El-Dessouky, H. Ettouney, Plastic/compact heat exchangers for single-effect desalination systems, Desalination 122 (1999) 271–289.
[30] M.M. Shah, A general correlation for heat transfer during film condensation inside pipes, Int. J. Heat Mass Transf. 22(4) (1979) 547–556.
[31] M. Ameri, S.S. Mohammadi, M. Hosseini, M. Seifi, Effect of design parameters on multi-effect desalination system specifications, Desalination 245(1–3) (September 2009) 266–283.
[32] Investigation of Local Absorption rates in Falling-Film Absorption. [Online]. Available from: http://stsl.gatech.edu/research-falling.html (accessed 16 February 2014).
[33] V. Gnielinski, New equations for heat and mass transfer in turbulent pipe and channel flow, Int. Chem. Eng. 16(2) (1976) 359–368.
[34] G. Nellis, S. Klein, Heat Transfer, Cambridge University Press, New York, NY, 2009.
[35] H.D. Baehr, K. Stephan, Heat and Mass Transfer, 2e, Springer, Berlin Heidelberg, 2006.
[36] L.M. Jiji, Heat Convection, 2e, Springer, Berlin Heidelberg, Berlin, Heidelberg, 2009.
[37] B.S. Petukhov, Heat transfer and friction in turbulent pipe flow with variable physical properties, Adv. Heat Transf. 6 (1970) 503–564.

[38] K.E. Herold, R. Radermacher, S.A. Klein, Absorption chillers and heat pumps, CRC Press, Taylor and Francis Group, Boca Raton, FL, 1996, pp. 113–144.
[39] I. Kyung, K.E. Herold, Y.T. Kang, Experimental verification of H_2O/LiBr absorber bundle performance with smooth horizontal tubes, Int. J. Refrig. 30(4) (June 2007) 582–590.
[40] ASHRAE, Thermodynamics and refrigeration cycles, in: 2013 ASHRAE Handbook: Fundamentals, American Society of Heating, Refrigeration and Air-Conditioning Engineers, Atlanta, GA, 2013. pp. 2.17–2.19.
[41] SimTechnology, IPSEpro Ver. 5.1, 2012. [Online]. Available from http://www.simtechnology.com/.
[42] W.E. Alnaser, B. Eliagoubi, A. Al-Kalak, H. Trabelsi, M. Al-Maalej, H.M. El-Sayed, M. Alloush, First solar radiation atlas for the Arab world, Renew. Energy 29 (7) (June 2004) 1085–1107.
[43] Y.A.G. Abdalla, M.K. Baghdady, Global and diffuse solar radiation in Doha (Qatar), Sol. Wind Technol. 2 (3–4) (January 1985) 209–212.
[44] H.T. El-Dessouky, H.M. Ettouney, Fundamentals of Salt Water Desalination, Elsevier Science, Amsterdam, 2002.
[45] A. Husain, K. Wangnick, A. Radif, Case Study on Planning a Large Scale Multistage Flash Desalination Plant, in Thermal Desalination Processes. Eolss Publishers, Oxford, UK, Encyclopedia of Desalination and Water Resources, 2004.

Appendix A

Specific enthalpy of the brine [44]

$$h_b = A_0 + 10^{-3}\left(A_1 t + A_2 t^2 + A_3 t^3 + A_4 t^4\right)$$

$$A_0 = 9.62964\, w_b - 431.2404\, w_b^2$$

$$A_1 = 1.000000433\,\left(4206.8 - 6619.7\, w_b + 12288\, w_b^2\right)$$

$$A_2 = 0.5000002164\,\left(-1.1262 + 54.178\, w_b - 227.19\, w_b^2\right)$$

$$A_3 = 0.3333334776\,\left(0.0120264 - 0.53566\, w_b + 1.8906\, w_b^2\right)$$

$$A_4 = 0.2500001082\,\left(0.68774 \times 10^{-6} + 0.1517 \times 10^{-2}\, w_b - 0.4268 \times 10^{-2}\, w_b^2\right)$$

Specific heat of the brine [44]

$$C_p = \quad 10^{-3}\left(A_0 + A_1\, t + A_2\, t^2 + A_3\, t^3\right)$$

$$A_0 = \quad 4206.8 - 6619.6\, w_b + 12288.0\, w_b^2$$

$$A_1 = -1.1262 + 54.1785\, w_b - 227.19\, w_b^2$$

$$A_2 = -0.0112026 - .53566\, w_b + 1.8906\, w_b^2$$

$$A_3 = 0.68774 \times 10^{-6} + 0.1517 \times 10^{-2}\, w_b - 0.44268 \times 10^{-2}\, w_b^2$$

Boiling point elevation [45]

$$T_{\mathrm{BPE}} = A_0 \cdot \mathrm{TDS} + A_1 \cdot \mathrm{TDS}^2 + \mathrm{A}_2 \cdot \mathrm{TDS}^3$$

$$A_0 = a_0 + b_0 \cdot T + c_0 \cdot T^2$$

$$A_1 = a_1 + b_1 \cdot T + c_1 \cdot T^2$$

$$A_2 = a_2 + b_2 \cdot T + c_2 \cdot T^2$$

$$a_0 = 82543.1 \times 10^{-6} \quad b_0 = 188.3 \times 10^{-6} \quad c_0 = 4.02 \times 10^{-6}$$

$$a_1 = -762.5 \times 10^{-6} \quad b_1 = 9.02 \times 10^{-6} \quad c_1 = -0.52 \times 10^{-6}$$

$$a_2 = 152.2 \times 10^{-6} \quad b_2 = -3.0 \times 10^{-6} \quad c_2 = 0.03 \times 10^{-6}$$